

Can neutrino-cooled accretion disk be an origin of gamma-ray bursts?

Kazunori Kohri and Shin Mineshige

Yukawa Institute for Theoretical Physics, Kyoto University, Kyoto, 606-8502, Japan

kohri@yukawa.kyoto-u.ac.jp, minesige@yukawa.kyoto-u.ac.jp

ABSTRACT

It is often considered that a massive torus with solar mass or so surrounding a stellar-mass black hole may be a central engine of a gamma-ray burst. We study the properties of such massive accretion tori (or disks) based on the α viscosity model. For surface density exceeding about 10^{20} g cm $^{-2}$, which realizes when about a solar-mass material is contained within a disk with a size of $\sim 5 \times 10^6$ cm, we find that (1) luminosity of photons is practically zero due to significant photon trapping, (2) neutrino cooling dominates over advective cooling, (3) pressure of degenerate electrons dominates over pressure of gas and photons, and (4) magnetic field strength exceeds the critical value of about 4×10^{13} G, even if we take 0.1 % of the equi-partition value. The possible observable quantum electrodynamical (QED) effects arising from super-critical fields are discussed. Most interestingly, photon splitting may occur, producing significant number of photons of energy below ~ 511 keV, thereby possibly suppressing e^\pm pair creation.

Subject headings: accretion, accretion disks — black hole physics — gamma-ray bursts — neutrinos

1. Introduction

Research on gamma-ray bursts (GRBs) has made rapid progress over the past decade, particularly after the discovery of afterglow by Beppo-SAX (see recent reviews by Mészáros, Rees, & Wijers 1999; Piran 2000; Mészáros 2001). The current common belief is that GRBs are the most energetic explosions which ever occurred in the Universe, releasing energy of $\sim 10^{51} - 10^{53}$ erg only in a few to few tens of seconds. It is also widely argued that GRBs result from the conversion of the kinetic energy of ultra-relativistic particles created within a fire ball. A relativistic fireball shock model was proposed to resolve the compactness problem and has had some success in explaining how the GRB and afterglow radiation arise (Rees & Mészáros 1992, 1994; Wijers & Galama 1999).

However, the central engines of GRBs creating initial hot plasma or extremely energetic particles are not well understood yet due mainly to the fact that they are hidden from our view. It is usually argued that relativistic phenomena should be somehow involved, since otherwise it is

difficult to explain huge fluence and rapid burst-like burst profiles. (Narayan, Paczyński & Piran 1992). Along this line, many interesting possibilities have been proposed so far, such as (1) mergers of double neutron star (NS) binaries or NS and BH (black hole) (Paczyński 1986, 1991; Goodman 1986; Eichler et al. 1989), (2) BH-WD (white dwarf) merger (Fryer et al. 1999); (3) BH-helium star merger (Fryer et al. 1999); (4) failed supernova (or collapsars, Woosley 1993; Paczyński 1998; MacFadyen & Woosley 1999), and (5) magnetar, rapidly spinning neutron star with extremely large magnetic fields (Usov 1992, 1994; Thompson 1994; Spruit 1999). It is of great importance to note that almost all the models (except for the magnetar hypothesis) predicts a similar configuration as an end result; namely, formation of a few solar mass black hole surrounded by a temporary debris torus (or disk) with mass of $0.01 - 1.0 M_{\odot}$ whose accretion can provide a sudden release of gravitational energy (Mészáros, Rees, & Wijers 1999). Then, the key issue will be to understand the properties of such a compact and massive disk associated with a huge mass accretion rate.

Accretion models for gamma-ray bursts were first considered by Narayan, Paczyński & Piran (1992), and recently discussed in more details by Popham, Woosley, & Fryer (1999) and Narayan, Piran, & Kumar, (2001, hereafter NPK). According to them, neutrino cooling dominates over radiative loss at very huge accretion rates (see, however, Chevalier 1996; see also Ruffert & Janka 1999 for a numerical simulation of a binary merger including neutrino losses. Therefore, such disks (or flows) are called as neutrino-dominated accretion flow (NDAF). In the present study, we elucidate the theory of NDAF based on the α viscosity prescription, paying special attention to their thermal structure and the implications of expected huge magnetic fields. We present the resultant equilibrium solutions and properties of neutrino-cooled disks in section 2. We then discuss the effects of huge magnetic fields and implications on neutrino emission in section 3. Final section is devoted to conclusions.

2. Structure of Neutrino-Cooled Disk

2.1. $\Sigma - T$ diagram

In this study we adopt the following basic equations based on the Newtonian dynamics, for simplicity (see, e.g., Kato, Fukue, & Mineshige 1998). We use the cylindrical coordinates, (r, φ, z) . Then, the mass conservation in the vertical and radial direction is, respectively, represented by

$$\rho = \frac{\Sigma}{2H} \quad \text{and} \quad \dot{M} = -2\pi r v_r \Sigma, \quad (1)$$

where ρ is the matter density, Σ is the surface density of the disk, H is the disk half-thickness, \dot{M} is the mass accretion rate, and v_r is the radial velocity (negative for inflow). The disk half-thickness is, from hydrostatic balance in the vertical direction, given by

$$H = c_s / \Omega, \quad (2)$$

where the (isothermal) sound velocity c_s is defined by

$$c_s \equiv \sqrt{p/\rho}, \quad (3)$$

with the pressure p . The angular velocity, Ω , is in the Newtonian approximation given by

$$\Omega = \sqrt{GM_{\text{BH}}/r^3}, \quad (4)$$

with G being the gravitational constant and M_{BH} being the black-hole mass. The pressure is composed of three terms:

$$p = p_{\text{rad}} + p_{\text{gas}} + p_{\text{d}}, \quad (5)$$

where p_{rad} is the radiation pressure, p_{gas} is the gas pressure of the nonrelativistic and non-degenerate particles, and p_{d} is the pressure of the degenerate particles. The radiation pressure is

$$p_{\text{rad}} = \frac{a}{6} g_* T^4, \quad (6)$$

where g_* is statistical degree of freedom in the radiation (=2 for γ , or 11/2 for γ and e^+e^- plasma) and a is the radiation constant. The gas pressure is

$$p_{\text{gas}} = \sum_i n_i k_{\text{B}} T, \quad (7)$$

where k_{B} is the Boltzmann constant, n_i is the number density of particle “ i ”, and the suffix i runs the nonrelativistic and non-degenerate particles at the temperature (e.g., e^- and nucleons at $T \lesssim m_{\text{e}} c^2/k_{\text{B}}$). The pressure of the degenerate particles is written as

$$p_{\text{d}} = p_{\text{d,nonrel}} + p_{\text{d,rel}}. \quad (8)$$

Then,

$$p_{\text{d,nonrel}} = \sum_{i=\text{nonrel}} \frac{1}{5} \left(\frac{6\pi^2}{g_i} \right)^{2/3} \frac{\hbar^2 n_i^{5/3}}{m_i}, \quad (9)$$

is for nonrelativistic particles which satisfy the condition of the degeneracy,

$$n_i \gg g_i (m_i k_{\text{B}} T / 2\pi\hbar^2)^{3/2}, \quad (10)$$

for $T \ll m_i c^2/k_{\text{B}}$ and $\mu_i \ll m_i c^2$ with their mass m_i , statistical degree of freedom g_i and their chemical potential μ_i , and

$$p_{\text{d,rel}} = \sum_{i=\text{rel}} \frac{1}{4} \left(\frac{6\pi^2}{g_i} \right)^{1/3} \hbar^2 c n_i^{4/3}, \quad (11)$$

is for relativistic particles which satisfy the condition of the degeneracy,

$$n_i \gg g_i (k_{\text{B}} T / \hbar c)^3 / \pi^2, \quad (12)$$

for $T \gg m_i c^2 / k_B$ or $\mu_i \gg m_i c^2$. In this study, for simplicity we assume the complete degeneracy whenever the above condition of the degeneracy is satisfied.

In Fig. 1, we plot the contours of the matter density on the (Σ, T) plane. From the figure we can read off the matter density. It also discriminates the regions where each pressure component is dominant and also the regions where electrons and/or nucleons are degenerate. We understand that degeneracy pressure is important at high density and low temperature regimes. Such regimes inevitably appear in very massive disks, and one can never neglect the contributions by degeneracy pressure in GRBs unlike the cases of binary systems or galactic centers. We also notice that one should distinguish the regime where only electrons are degenerate from the one where both electrons and nucleons are degenerate.

2.2. chemical potential of electrons

When electrons are degenerate, there emerges an important consequence on the process of neutrino emission, that is, e.g., since the pair creation of electron and positron in the electromagnetic thermal bath is suppressed by the charge neutrality (see below), the neutrino emission is also suppressed (This is not discussed in NPK). The electron chemical potential μ_e is determined by the condition of charge neutrality,

$$n_p = n_{e^-} - n_{e^+}, \quad (13)$$

with the number density of electron and positron,

$$n_{e^-} = \frac{1}{\hbar^3 \pi^2} \int_0^\infty dp p^2 \frac{1}{e^{(\sqrt{p^2 c^2 + m_e^2 c^4} - \mu_e)/k_B T} + 1}, \quad (14)$$

$$n_{e^+} = \frac{1}{\hbar^3 \pi^2} \int_0^\infty dp p^2 \frac{1}{e^{(\sqrt{p^2 c^2 + m_e^2 c^4} + \mu_e)/k_B T} + 1}. \quad (15)$$

In the following sections, it is convenient to introduce a dimensionless chemical potential of electrons which is defined by

$$\eta_e = \mu_e / k_B T. \quad (16)$$

Then, the complete degeneracy of electrons corresponds to $\eta_e \gg 1$, and the charge neutrality in Eq. (13) becomes

$$n_p \simeq n_{e^-} \simeq \frac{1}{3\pi^2} \left(\frac{\mu_e}{\hbar c} \right)^3. \quad (17)$$

The chemical potentials of protons and neutrons are defined through the relation,

$$n_p = \frac{1}{\hbar^3 \pi^2} \int_0^\infty dp p^2 \frac{1}{e^{(\sqrt{p^2 c^2 + m_p^2 c^4} - \mu_p)/k_B T} + 1}, \quad (18)$$

$$n_n = \frac{1}{\hbar^3 \pi^2} \int_0^\infty dp p^2 \frac{1}{e^{(\sqrt{p^2 c^2 + m_n^2 c^4} - \mu_n)/k_B T} + 1}. \quad (19)$$

If the nucleons are not degenerate, we have

$$n_i = 2 \left(\frac{m_i k_B T}{2\pi\hbar^2} \right)^{3/2} e^{-(m_i c^2 - \mu_i)/k_B T}, \quad (20)$$

for $i = p, n$. On the other hand, if nucleons are degenerate, we have

$$n_i = \frac{1}{3\pi^2} \left(\frac{2\tilde{\mu}_i m_i}{\hbar^2} \right)^{3/2}, \quad (21)$$

for the complete degenerate limit with

$$\tilde{\mu}_i = \mu_i - m_i c^2. \quad (22)$$

In this study, we did not directly solve the exact equation in Eq. (13) to derive the chemical potential of electrons. Instead, we performed the following approximated computations in the complete-degeneracy regime ($\eta_e \gg 1$). As will be shown later, nucleons are in β -equilibrium at a high temperature $T \gtrsim 5.0 \times 10^{10} \text{K} (\alpha/0.1)^{1/5} (r/4r_g)^{-3/10} (M_{\text{BH}}/3M_{\odot})^{-1/5}$ where the neutrino emissions are effective and mainly contribute to the cooling process. Then, the chemical equilibrium is realized,

$$\mu_p + \mu_e = \mu_n, \quad (23)$$

or

$$\tilde{\mu}_p + \mu_e - Q = \tilde{\mu}_n, \quad (24)$$

where $Q = (m_n - m_p)c^2 \simeq 1.29 \text{ MeV}$. In the regime where only electrons are degenerate, β -equilibrium means

$$\frac{n_p}{n_n} = \exp [(Q - \mu_e)/(k_B T)]. \quad (25)$$

The electron fraction $Y_e \equiv n_p/(n_p + n_n)$ is related with the above ratio by $Y_e = 1/(1 + (n_p/n_n)^{-1})$. Combined with the condition of the charge neutrality, i.e., Eq. (17), we may only solve the equation,

$$\frac{\rho}{m_p} \exp(-\mu_e/(k_B T)) = \frac{1}{3\pi^2} \left(\frac{\mu_e}{\hbar c} \right)^3, \quad (26)$$

for $\mu_e \gg k_B T \gg Q$. On the other hand, it is relatively easy for us to calculate μ_e in the regime where both electrons and nucleons are degenerate. From the charge neutrality (Eq. (17)) and chemical equilibrium (Eq.(24)), we find that $\mu_e \sim \tilde{\mu}_n \gg \tilde{\mu}_p$ for $k_B T \ll \mu_e < \mathcal{O}(10^2) \text{ MeV}$. Then, from Eq. (21) we can approximately estimate the chemical potential of electrons as

$$\mu_e \simeq \tilde{\mu}_n \quad (27)$$

$$\simeq 6.628 \text{ MeV} (\rho/10^{13} \text{g cm}^{-3})^{2/3}, \quad (28)$$

in the complete-degeneracy limit of both electrons and nucleons.

We also plot the contours of the chemical potential of electrons in units of MeV ($\mu_{e,\text{MeV}} = 10$, and 20) in Fig. 1. The chemical potential of electrons play important roles to estimate the emission rates of neutrinos which will be discussed in the next subsection.

2.3. Heating and cooling rates

The most important relation in the accretion disk theory is the energy balance between the heating and cooling processes. Distinct branches (such as a standard disk or a slim disk, etc.) appear because of different heating and/or cooling sources being dominant. According to the standard α viscosity model, we express the vertically integrated heating rate (over a half thickness, H) as

$$Q^+ = Q_{\text{vis}}^+ = \frac{9}{8} \nu \Sigma \Omega^2, \quad (29)$$

where Q_{vis}^+ denotes the viscous heating rate per unit surface area, the kinetic viscosity ν is related to the viscosity parameter α by

$$\nu = \frac{2}{3} \alpha c_s H. \quad (30)$$

If we assume the angular momentum conservation, we obtain

$$\nu \Sigma = \frac{\dot{M}}{3\pi} \left(1 - \sqrt{\frac{r_{\text{in}}}{r}} \right), \quad (31)$$

where r_{in} is the radius of the inner edge of the disk ($= 3 r_g$). From Eqs. (29), (30) and (31), we can relate the heating rate with the mass accretion rate;

$$\dot{M} = \frac{8\pi}{3} \Omega^{-2} \left(1 - \sqrt{\frac{r_{\text{in}}}{r}} \right)^{-1} Q^+. \quad (32)$$

The cooling rate is, on the other hand, summation of three major contributions;

$$Q^- = Q_{\text{rad}}^- + Q_{\text{adv}}^- + Q_{\nu}^-, \quad (33)$$

where Q_{rad}^- is the radiative cooling rate, Q_{adv}^- is the advective energy transport (Abramowicz et al. 1988), and Q_{ν}^- is the cooling rate due to neutrino loss. Note that instead of including advective energy transport in the energy equation NPK adopted the view of CDAF (convection-dominated accretion flow; Igumenshchev, Abramowicz, & Narayan 2000, Narayan, Igumenshchev, & Abramowicz, 2000, Quataert & Gruzinov 2000). We, in the present study, retain the classical picture based on the (vertically) one-zone treatment (e.g., Kato, Fukue, & Mineshige 1998), since it is not yet clear if CDAF provides precise description to the flow structure not only in the low-luminosity regimes but also in the hyper-accretion regimes. However, such a distinction is not essential here, since we are concerned with the regimes of even higher accretion rates, in which neutrino emission is substantial (discussed later).

The radiative cooling rate is

$$Q_{\text{rad}}^- = \frac{g_* \sigma_s T^4}{2\tau_{\text{tot}}}, \quad (34)$$

where $\sigma_s = \pi^2 k_B^4 / (60 \hbar^3 c^2)$ is the Stefan-Boltzmann constant and the optical depth, τ_{tot} , is given by

$$\tau_{\text{tot}} = \kappa_R \rho H = \frac{\kappa_R \Sigma}{2}, \quad (35)$$

with κ_R being the Rosseland-mean opacity,

$$\kappa_R = 0.40 + 0.64 \times 10^{23} \left(\frac{\rho}{\text{g cm}^{-3}} \right) \left(\frac{T}{\text{K}} \right)^{-3} \text{g}^{-1} \text{cm}^2. \quad (36)$$

The advective cooling rate is given by (Kato, Fukue, & Mineshige 1998),

$$Q_{\text{adv}}^- = \Sigma T v_r \frac{ds}{dr}, \quad (37)$$

where the radial velocity is $v_r = -\dot{M}/(2\pi r \Sigma)$ and s denotes entropy per particle,

$$s = (s_{\text{rad}} + s_{\text{gas}}) / \rho. \quad (38)$$

Here, the entropy density of the radiation is

$$s_{\text{rad}} = \frac{2}{3} a g_* T^3, \quad (39)$$

and entropy density of the gas (i.e., nonrelativistic particles) is

$$s_{\text{gas}} = \sum_i n_i \left(\frac{5}{2} + \ln \left[\frac{g_i}{n_i} \left(\frac{m_i T}{2\pi} \right)^{3/2} \right] \right), \quad (40)$$

where the suffix i runs over nonrelativistic nucleon and electron, g_i is the statistical degree of freedom of the particle. In the following, we approximated ds/dr as s/r . Note that since the entropy of degenerate particles is small in the complete-degeneracy limit, we neglect it here.

The neutrino cooling rate is composed of four terms;

$$Q_{\nu}^- = (\dot{q}_{Ne} + \dot{q}_{e^+e^-} + \dot{q}_{\text{brems}} + \dot{q}_{\text{plasmon}}) H, \quad (41)$$

where \dot{q}_{Ne} is the electron-positron capture rate by a nucleon “N”, $\dot{q}_{e^+e^-}$ is the electron-positron pair annihilation rate, \dot{q}_{brems} is the nucleon-nucleon bremsstrahlung rate, and \dot{q}_{plasmon} is the rate of plasmon decays. Note that NPK considered only the case of the non-degenerate electrons in first two terms on the right-hand side of Eq. (41). However, the case of the degenerate electrons in the first two terms and the other two terms could be also important.

The electron-positron capture rate is represented by two terms:

$$\dot{q}_{Ne} = \dot{q}_{p+e^- \rightarrow n+\nu_e} + \dot{q}_{n+e^+ \rightarrow p+\bar{\nu}_e}, \quad (42)$$

with

$$\dot{q}_{p+e^- \rightarrow n+\nu_e} = \frac{G_F^2}{2\pi^3 \hbar^3 c^2} (1+3g_A) n_p \int_Q^\infty dE_e E_e \sqrt{E_e^2 - m_e^2 c^4} (E_e - Q)^3 \frac{1}{e^{(E_e - \mu_e)/k_B T} + 1}, \quad (43)$$

$$\dot{q}_{n+e^+ \rightarrow p+\bar{\nu}_e} = \frac{G_F^2}{2\pi^3 \hbar^3 c^2} (1+3g_A) n_n \int_{m_e c^2}^\infty dE_e E_e \sqrt{E_e^2 - m_e^2 c^4} (E_e + Q)^3 \frac{1}{e^{(E_e + \mu_e)/k_B T} + 1} \quad (44)$$

where G_F is the Fermi coupling constant ($= 2.302 \times 10^{-22} \text{ cm MeV}^{-1}$), and g_A is the axial-vector coupling constant of nucleon (~ 1.39) which is normalized by the experimental value of neutron lifetime $\tau_n \simeq 886.7$ s. In the non-degeneracy limit ($\mu_e \ll k_B T$), it is easily estimated by

$$\dot{q}_{Ne} = 9.2 \times 10^{33} \text{ erg cm}^{-3} \text{ s}^{-1} \left(\frac{T}{10^{11} \text{ K}} \right)^6 \left(\frac{\rho}{10^{10} \text{ g cm}^{-3}} \right). \quad (45)$$

On the other hand, it is a little complicated to estimate the electron capture rate in the electron-degeneracy regime. In the only electron-degeneracy regime, we have

$$\dot{q}_{Ne} = 1.1 \times 10^{31} \eta_e^9 \text{ erg cm}^{-3} \text{ s}^{-1} \left(\frac{T}{10^{11} \text{ K}} \right)^9, \quad (46)$$

for complete degeneracy limit of electrons. Note that in this limit, independently we can also obtain the chemical potential of electrons by the balance between the two dominant weak interaction rates, i.e., $\dot{q}_{p+e^- \rightarrow n+\nu_e} = 5.3 \times 10^{30} \eta_e^9 \text{ erg cm}^{-3} \text{ s}^{-1} (T/10^{11} \text{ K})^9$ and $\dot{q}_{n+e^+ \rightarrow p+\bar{\nu}_e} = 2.6 \times 10^{37} \exp(-m_e/(k_B T)) \exp(-\eta_e) \text{ erg cm}^{-3} \text{ s}^{-1} (\rho/10^{13} \text{ g cm}^{-3}) (T/10^{11} \text{ K})^6$. Compared with the chemical potential which was obtained in Eq (26) where we assumed the complete β -equilibrium, they agree with each other just within a few percent, e.g., $\eta_e \simeq 3.5$ at $\rho = 10^{13} \text{ g cm}^{-3}$ and $T = 10 \text{ MeV}/k_B$. Therefore, our assumptions of the complete-degeneracy limits would be reasonable.

When both electrons and nucleons are degenerate, the reactions $p+e^- \leftrightarrow n+\nu_e$ are suppressed by the Fermi blocking of degenerate nucleons in the final states. Then, for example the dE_e integration in Eq. (43) is limited as $[\mu_e, \infty]$, and we approximately obtain the relatively small cooling rate, $\dot{q}_{Ne} = 5.0 \times 10^{32} \eta_e^7 \text{ erg cm}^{-3} \text{ s}^{-1} (T/10^{11} \text{ K})^9$. Compared with Eq. (46), of course, we find that this rate is smaller by a factor of $1/\eta_e^2$ in the complete degeneracy regime, i.e., $\eta_e \gg 1$.

The electron-positron pair annihilation rate through $e^+ + e^- \rightarrow \nu + \bar{\nu}$ is

$$\dot{q}_{e^+e^-} = 4.8 \times 10^{33} \text{ erg cm}^{-3} \text{ s}^{-1} \left(\frac{T}{10^{11} \text{ K}} \right)^9, \quad (47)$$

in the non-degeneracy regime, e.g., see Itoh et al. (1989, 1990). When the electrons are degenerate, the electron-positron pair annihilation rate is too small to compete the other cooling process, and we can neglect it.

The nucleon-nucleon bremsstrahlung rate through $n+n \rightarrow n+n+\nu+\bar{\nu}$ is represented by

$$\dot{q}_{\text{brems}} = 3.4 \times 10^{33} \text{ erg cm}^{-3} \text{ s}^{-1} \left(\frac{T}{10^{11} \text{ K}} \right)^8 \left(\frac{\rho}{10^{13} \text{ g cm}^{-3}} \right)^{1/3}, \quad (48)$$

in the degeneracy regime of nucleons (Hannestad & Raffelt 1998), and

$$\dot{q}_{\text{brems}} = 1.5 \times 10^{33} \text{ erg cm}^{-3} \text{ s}^{-1} \left(\frac{T}{10^{11} \text{ K}} \right)^{5.5} \left(\frac{\rho}{10^{13} \text{ g cm}^{-3}} \right)^2, \quad (49)$$

in the non-degeneracy regime of nucleons (Hannestad & Raffelt 1998; Burrows et al. 2000).

It is also known that the plasmon decay is effective in high densities and high electron degeneracy region (Schinder et al. 1987). The decay rate of the transverse plasmons which are normal photons interacting with the electron gas through $\tilde{\gamma} \rightarrow \nu_e + \bar{\nu}_e$ is estimated by Ruffert, Janka & Schäfer (1996) as

$$\dot{q}_{\text{plasmon}} = 1.5 \times 10^{32} \text{ erg cm}^{-3} \text{ s}^{-1} \left(\frac{T}{10^{11} \text{ K}} \right)^9 \gamma_p^6 e^{-\gamma_p} (1 + \gamma_p) \left(2 + \frac{\gamma_p^2}{1 + \gamma_p} \right), \quad (50)$$

where $\gamma_p = 5.565 \times 10^{-2} \sqrt{(\pi^2 + 3\eta_e^2)/3}$. In particular, $\tilde{\gamma} \rightarrow \nu_e + \bar{\nu}_e$ is a dominant process by a factor of ~ 163 compared with the other flavor ($\rightarrow \nu_\mu \bar{\nu}_\mu$ or $\nu_\tau \bar{\nu}_\tau$).

Note that in NPK only Eqs. (45) and (47) cases were considered in \dot{q}_ν . To see what component of the cooling rates mainly contributes to the process, in Fig. 2 we plot the most dominant one on the (Σ, T) plane. It is interesting to note that the region where advective energy transport dominates covers a rather wide, large Σ and high T part of the $\Sigma - T$ diagram. This is because $Q_{\text{adv}} (\propto T^{16})$ has a stronger T dependence than $Q_{\text{rad}} (\propto T^4)$ (shown later). Also notice that neutrino cooling is essential only at very high temperatures ($T \gtrsim 10^{11} \text{ K}$) and very high matter density $\rho \gtrsim 10^{10} - 10^{13} \text{ g cm}^{-3}$. The striped region represents the place where heavy elements are produced which are expected from the point of view in the equation of state of nuclear matter (Shen et al, 1998; Ishizuka, Ohnishi & Sumiyoshi 2002). Here, we adopt the case of the electron fraction $Y_e \simeq 0.1$ which the numerical simulations of coalescing neutron stars predict, e.g., see Ruffert et al (1997). Note that the left side of the boundary of the striped region is just virtual one. Of course, the tail realistically continues to the left further. As a result, there exist just a small amount of free nucleons. Namely, the neutrino processes which we consider in this study no longer become effective there.

Next, in Fig. 3, we plot the heating and cooling rates as a function of the temperature for some representative values of surface density: (a) $\Sigma = 10^{3.5} \text{ g cm}^{-2}$, (b) $\Sigma = 10^8 \text{ g cm}^{-2}$, and (c) $\Sigma = 10^{20} \text{ g cm}^{-2}$. In Fig. 3(a), we find three intersection points. They contain two points in which the energy balance is realized due to the radiative or advective cooling processes. As for Fig. 3(b), there exists only one intersection point in which the energy balance is realized because of the advective cooling processes. It is interesting that in Fig. 3(c), a new branch of the energy balance appears at $T \gtrsim m_e c^2/k_B$, since the neutrino-cooling process becomes effective. By plotting only the values at those intersecting points on the (Σ, T) or (Σ, \dot{M}) plane for various values of Σ , we obtain a sequence of the thermal equilibrium solutions; that is the thermal equilibrium curve.

2.4. Various time scales

Here it is necessary for us to check the time scale of the physical processes of the neutrino cooling. The dynamical timescale is represented by the accretion time,

$$\tau_{\text{acc}} \equiv \frac{1}{\alpha} \sqrt{\frac{r^3}{GM_{\text{BH}}}} \left(\frac{r}{H}\right)^2, \quad (51)$$

$$\simeq 1.3 \times 10^{-2} \text{ s} \left(\frac{\alpha}{0.1}\right)^{-1} \left(\frac{r}{4r_g}\right)^{3/2} \left(\frac{M_{\text{BH}}}{3M_{\odot}}\right), \quad (52)$$

where we assumed that the disk half-thickness is approximately $H \sim r/2$. On the other hand, the time scale of weak interaction of a nucleon off the background electrons and positrons is estimated by

$$\tau_{\beta} \equiv (\sigma_{Ne} n_e c)^{-1} \quad (53)$$

$$\sim 1.0 \times 10^{-4} \text{ s} \left(\frac{T}{10^{11}\text{K}}\right)^{-5}, \quad (54)$$

where we assume that the cross section is $\sigma_{Ne} \sim G_F^2 (k_B T)^2$, and the electron number density is $n_e \sim (k_B T / \hbar c)^3$. Then, the condition $\tau_{\beta} \leq \tau_{\text{acc}}$ is realized when the following relation is satisfied,

$$T \geq 3.8 \times 10^{10} \text{K} \left(\frac{\alpha}{0.1}\right)^{1/5} \left(\frac{r}{4r_g}\right)^{-3/10} \left(\frac{M_{\text{BH}}}{3M_{\odot}}\right)^{-1/5}. \quad (55)$$

The interaction rate of a neutrino off the background nucleons is roughly given by

$$\Gamma_{N\nu} \sim G_F^2 (k_B T)^2 n_N c, \quad (56)$$

with the nucleon density n_N . Since $H \sim r/2$, the ratio of the interaction time ($1/\Gamma_{N\nu}$) and the neutrino crossing time (H/c) is estimated by

$$\Gamma_{N\nu} \times H/c \simeq 42.6 \left(\frac{T}{10^{11}\text{K}}\right)^2 \left(\frac{\rho}{10^{13} \text{g cm}^{-3}}\right) \left(\frac{r}{4r_g}\right) \left(\frac{M_{\text{BH}}}{3M_{\odot}}\right). \quad (57)$$

Since the nucleon to electron-positron ratio is $n_N/n_e \sim \mathcal{O}(10)(\rho/10^{13} \text{g cm}^{-3})/(T/10^{11}\text{K})^{-3}$, we find that the neutrino interaction is rapid enough to realize β -equilibrium which we have assumed in the previous subsections. When $\Gamma_{N\nu} H/c$ is greater than unity, we should modify the neutrino cooling rate in Eq. (41). To correctly estimate it in that case, we should divide the right-hand side of Eq. (41) by $\Gamma_{N\nu} H/c$. However, since the neutrino cooling rate becomes $\mathcal{O}(10^2)$ times larger than the heating rate suddenly at intersection points between the cooling and the heating rates, to estimate the equilibrium curve, our simple treatments in the previous section are not so wrong and the results are not changed.

Next, we estimate the vertical diffusion time of neutrinos. It is given by

$$\tau_{\text{diff}} \equiv \frac{(H/c)^2}{\Gamma_{N\nu}^{-1}}, \quad (58)$$

$$\simeq 2.6 \times 10^{-3} \text{ s} \left(\frac{T}{10^{11} \text{ K}} \right)^2 \left(\frac{\rho}{10^{13} \text{ g cm}^{-3}} \right) \left(\frac{r}{4 r_g} \right)^2 \left(\frac{M_{\text{BH}}}{3 M_{\odot}} \right)^2. \quad (59)$$

Compared it with Eq. (51), the condition of $\tau_{\text{diff}} \leq \tau_{\text{acc}}$ is translated into

$$T \leq 2.3 \times 10^{11} \text{ K} \left(\frac{\alpha}{0.1} \right)^{-1/2} \left(\frac{\rho}{10^{13} \text{ g cm}^{-3}} \right)^{-1/2} \left(\frac{r}{4 r_g} \right)^{-1/4} \left(\frac{M_{\text{BH}}}{3 M_{\odot}} \right)^{-1/2}. \quad (60)$$

Therefore, the neutrino cooling process is effective and realistic in the equilibrium solutions of the accretion disk at a high temperature $T \sim 10^{11} \text{ K}$ and a high density $\rho \sim 10^{13} \text{ g cm}^{-3}$ which will be studied in the next subsection.

2.5. Thermal Equilibrium Solutions

According to the procedure discussed in Sec. 2.3, we can find the thermal equilibrium solutions; that is, intersecting points of the heating and cooling curves. In Fig. 4 we plot them on the (Σ, T) plane for $r = 4 r_g$ (left panel) and for $r = 40 r_g$ (right panel), respectively. In the parameter region where neutrino cooling is effective, the dominant processes are the electron capture rate ($N + e \rightarrow N' + \nu$).

Using Eq. (32), we can also express the mass accretion rate \dot{M} at the intersection points as a function of Σ . The thermal equilibrium curves on the (Σ, \dot{M}) plane are plotted in Fig. 5. Here, mass accretion rate is normalized by the critical mass accretion rate,

$$\dot{M}_{\text{crit}} = 16 L_{\text{Edd}} / c^2, \quad (61)$$

where L_{Edd} is the Eddington luminosity,

$$L_{\text{Edd}} = 4\pi G M_{\text{BH}} m_{\text{p}} c / \sigma, \quad (62)$$

with proton mass m_{p} and the cross section σ of the matter and the radiation through the electromagnetic scattering, i.e., $L_{\text{Edd}} / c^2 \simeq 7.3 \times 10^{-17} M_{\odot} \cdot \text{s}^{-1} (\sigma / \sigma_{\text{T}})^{-1} (M_{\text{BH}} / M_{\odot})$ with the Thomson cross section $\sigma_{\text{T}} \simeq 0.6652 \text{ mb}$.

There are 5 distinct branches seen in these plots (see Table 1). In the lower-left parts of both figures, the equilibrium sequence has an **S** shape (see Abramowicz et al. 1988), which arises because of changes in sources of pressure (gas and radiation pressure) and in sources of cooling (radiation and advection). In the upper branch of the **S** shape, advective energy transport takes over radiative cooling. Then, generated photons inside the disk take long time to go out from the disk surface so that photons are advected inward and are finally swallowed by a central black

hole with accreting matter. Then, disk luminosity is largely reduced. Such trapping effects should occur in branches III and IV with even higher \dot{M} . Neutrino cooling is dominant only in the high temperature and density regimes (branch V), in which neutrinos, instead of radiation, can carry away the generated energy inside the disk. In branch V of Table 1, we wrote Q_ν^- in the case that only electrons are degenerate. On the other hand, in the case that both electrons and nucleons are degenerate, Q_ν^- becomes smaller by a factor of $1/\eta_e^2$. Then, the thermal equilibrium solution is just realized on the line of the condition of nucleon degeneracy. Namely, the $T-\Sigma$ relation of the branch V coincides with that of nucleon degeneracy. In the intermediate branch (IV) still advective cooling is dominant, however, note that entropy which is transported by advection is contributed by non-degenerate nucleons, since entropy of degenerate particles is little.

It is interesting to examine the stability of each branch. The criterion for the thermal instability is

$$\left(\frac{dQ^+}{dT} \right)_\Sigma > \left(\frac{dQ^-}{dT} \right)_\Sigma, \quad (63)$$

whereas that for the viscous (secular) instability is

$$\left(\frac{d\dot{M}}{d\Sigma} \right)_{Q^+ = Q^-} < 0, \quad (64)$$

(see, e.g., Kato, Fukue, & Matsumoto 1998). We understand immediately from Table 1 that only branch II (radiation pressure-dominant standard disk branch) is unstable for both modes and all other branches, including the NDAF branch, are stable for any modes, as already noted by NPK.

2.6. Properties of Neutrino-Cooled Disks

From the equilibrium solutions found in Sec. 2.5, we derive the following expressions for the temperature and density on the equatorial plane and for the corresponding mass-accretion rates as functions of radius for a given value of Σ :

$$T = 1.1 \times 10^{11} \text{ K} \left(\frac{\Sigma}{10^{20} \text{ g cm}^{-2}} \right)^{4/7} \left(\frac{r}{4 r_g} \right)^{-6/7} \left(\frac{M_{\text{BH}}}{3 M_\odot} \right)^{2/7}, \quad (65)$$

$$\rho = 2.3 \times 10^{13} \text{ g cm}^{-3} \left(\frac{\Sigma}{10^{20} \text{ g cm}^{-2}} \right)^{6/7} \left(\frac{r}{4 r_g} \right)^{-9/7} \left(\frac{M_{\text{BH}}}{3 M_\odot} \right)^{3/7}, \quad (66)$$

and

$$\dot{M} = 1.1 \times 10^{17} \dot{M}_{\text{crit}} \left(\frac{\alpha}{0.1} \right) \left(\frac{\Sigma}{10^{20} \text{ g cm}^{-2}} \right)^{9/7} \left(\frac{r}{4 r_g} \right)^{15/14} \left(\frac{M_{\text{BH}}}{3 M_\odot} \right)^{-5/14}. \quad (67)$$

Note that NPK derived similar expressions but in terms of the disk mass, M_{disk} , and the size of the initial torus, R_{out} , which are roughly related to surface density as

$$\Sigma \approx \frac{2M_{\text{disk}}}{\pi b R_{\text{out}}^2} \sim \frac{10^{20}}{b} \text{g cm}^{-2} \left(\frac{M_{\text{disk}}}{M_{\odot}} \right) \left(\frac{R_{\text{out}}}{5 \times 10^6 \text{cm}} \right)^{-2}, \quad (68)$$

where b is a constant of the order of unity, which varies, depending on the geometry of the initial torus and we assumed uniform surface density distribution. We thus understand that neutrino cooling dominates only if a solar-mass material is contained within a disk with a size of $\sim 5 \times 10^6$ cm. In other words, if the disk mass is less or if the disk size is larger, neutrino cooling never becomes dominant. This constraint is more severe than that obtained by NPK.

By comparing the left and right panels in Fig. 4, we notice that even at such a high surface density as $\Sigma \sim 10^{20} \text{g cm}^{-2}$, the neutrino cooling does not become dominant at a somewhat larger radius (i.e., $r \gtrsim 40 r_g$). This also supports the claim by NPK that NDAF solution only appears in a rather compact region around the center.

We can get a crude approximation for the strength of magnetic fields, by using the above results. The equi-partition field strength, for which magnetic energy is equal to gas energy, is

$$\begin{aligned} B_{\text{eq}} &= \left(\frac{8\pi\rho k_B T}{m_p} \right)^{1/2} \\ &\simeq 7.3 \times 10^{16} \text{G} \left(\frac{\alpha}{0.1} \right)^{1/12} \left(\frac{\Sigma}{10^{20} \text{g cm}^{-2}} \right)^{5/7} \left(\frac{r}{4 r_g} \right)^{-15/14} \left(\frac{M_{\text{BH}}}{3 M_{\odot}} \right)^{5/14}. \end{aligned} \quad (69)$$

Therefore, the strength of the magnetic field is very likely to exceed the critical value (e.g. Mészáros 1992),

$$B_{\text{crit}} \equiv \frac{m_e^2 c^3}{e \hbar} \simeq 4.4 \times 10^{13} \text{ G}, \quad (70)$$

even if the fields strength is only 0.1 % of the equi-partition value (for which magnetic energy is only 10^{-4} % of the particle energy). It is interesting to note that equilibrium B value is about the critical field for the proton,

$$B_{\text{crit,p}} = (m_p/m_e) B_{\text{crit}} \simeq 8 \times 10^{16} \text{ G}. \quad (71)$$

Then various QED (quantum-electrodynamics) effects should manifest themselves (see the next section).

3. Discussion

3.1. CDAF and slim disk

The present study is similar to that by NPK, although there are some differences. We newly take into account the effects of the electron and nucleon degeneracy in neutrino cooling processes.

The resultant disk density and temperature differ in the neutrino-dominated regimes. In the present study, we also take the slim-disk picture, instead of the CDAF picture adopted by NPK, at moderately large Σ (and thus \dot{M}) ranges. As mentioned above, the properties of the hyper-critical accretion flow is not yet clear, since full multi-dimensional simulations coupled with radiation hydrodynamics (RHD) and possibly with magnetohydrodynamics (MHD) are finally necessary to settle on this issue. Probably convection plays a key role there (Agol et al. 2001), but RHD simulations so far made in the hyper-critical regimes are based on the approximation of the flux-limited diffusion (e.g. Eggum, Coroniti, & Katz 1988; Fujita & Okuda 1998), which may not hold within highly turbulent media. Also, magnetic reconnection, which is not easy to simulate in realistic situations with extremely high magnetic Reynolds number, seems to play an important role (see below).

Our conclusion basically agrees with that by NPK in that NDAF appears at small radii only for high $M_{\text{disk}}/r_{\text{out}}^3$ cases. NPK concluded that models involving the mergers of BH-NS binaries and of NS-NS binaries are favored to explain short GRBs because then the flow is likely to be NDAF. However, our condition for the NDAF we found is more stringent than they found and may not be generally satisfied.

NPK also argue that the mergers of BH-WD binaries and BH-helium star binaries are difficult to explain GRBs for the following reason. Such mergers will create disks with large dimensions, thus being unable to reach the NDAF regimes but leading to the formation of CDAF. Then, convective motion mostly transports energy outward, thereby liberating little energy at small radii. It is thus unlikely to cause violent explosions like GRBs. However, we would like to point out that the flow pattern is rather uncertain in the presence of magnetic fields.

If there are strong magnetic fields with poloidal (vertical) components, for example, formation of outflow (or jet) is unavoidable (e.g. Blandford & Payne 1982; Kudoh, Matsumoto, & Shibata 1998), and such outflowing matter can produce enormous amount of synchrotron photons. Magnetic reconnections, giving rise to intense flare emission, may also occur. That is, mergers of BH and WD or helium star cannot be rejected as possible origins of GRBs. More careful discussion is needed regarding this issue.

3.2. Proof of $p_{\text{rad}} > p_{\text{gas}}$ in electron non-degeneracy

There are some discrepancies in the results between the present study and NPK. Those mainly come from a difference in the method. In NPK, for example, they analytically studied the scaling law of physical parameters in NDAF in two regimes, i.e., i) the gas pressure-dominated regime, and ii) the degeneracy pressure-dominated regime. Here, we show that gas pressure never becomes dominant whenever electrons are not degenerate at $T \gtrsim m_e c^2/k_B$. Namely only when electrons are degenerate, either gas pressure or degeneracy pressure can become dominant, i.e., the case i) is not realized in electron non-degeneracy.

Using Eqs. (6) and (7) with the condition $n_p \sim n_n$, we obtain the relation,

$$p_{\text{rad}}/p_{\text{gas}} \simeq 13.02 \left(\frac{\rho}{10^7 \text{g cm}^{-3}} \right)^{-1} \left(\frac{T}{\text{MeV}} \right)^3. \quad (72)$$

On the other hand, the non-degeneracy condition for relativistic electrons, see Eq. (12), is represented by

$$\left(\frac{\rho}{10^7 \text{g cm}^{-3}} \right)^{-1} \left(\frac{T}{\text{MeV}} \right)^3 \gg 0.1142. \quad (73)$$

From Eqs. (72) and (73), we see that the following relation is always realized,

$$p_{\text{rad}} \gg p_{\text{gas}}, \quad (74)$$

in the non-degenerate electron regime at $T \gtrsim m_e c^2/k_B$.

3.3. Expected QED effects arising due to super-critical magnetic fields

When the field strength exceeds the critical value ($\gtrsim \mathcal{O}(10^{13})$ G), quantum electrodynamical processes become important. Then, as it were, magnetic fields themselves behave as “particles” in the strongly magnetized vacuum, thus producing several unique features. For example, strong magnetic fields induce large energy splitting of Landau levels, large refractive indices of photons, photon splitting effect, and so on (see, e.g., Adler 1971; Shabad 1975; Melrose & Stoneham 1976; Chistyakov et al. 1998; Kohri & Yamada 2002a). In particular, the photon splitting effect is interesting, when we consider the present model of the hyper-critical accretion disk to a central engine of GRBs. That is because if the rate of photon splitting ($\gamma \rightarrow 2\gamma$) is larger than that of e^\pm pair production ($\gamma + \gamma \rightarrow e^+ + e^-$), high energy photons with their energy $E_\gamma \gg \text{MeV}$ can lose kinetic energy rapidly and produce a lot of soft photons ($E_\gamma \lesssim 0.511 \text{MeV}$) without producing copious electron-positron pairs. Then, it may be possible to produce a fire ball as a source of GRB without requiring a large Lorentz factor.

Unfortunately, however, any concrete values of the photon splitting rate near the threshold energy of the pair production has not been calculated precisely except for some formal formulations (Adler 1971; Shabad 1975; Melrose & Stoneham 1976). The numerical study above the threshold is currently underway (Kohri & Yamada 2002b) and needs further attention.

In addition, radiative processes in a ultra-magnetized plasma are inherently complicated and we are still far away from having the basic physics under control. At the enormous densities we are dealing with the optical depth is huge, so radiative transfer must be solved. Therefore, the above predictions may be premature at present. Only a detailed radiative transfer calculation, which is outside the present capabilities of numerical codes, could address this point.

3.4. Detectability of neutrinos from NDAFs

As we have shown in the previous sections, we expect that a lot of neutrinos would be emitted from NDAF. It is thus of great importance to check whether the signals of the neutrinos are detectable or not in GRB events. Moreover, it is also informative to find some correlations between neutrino emission and photon emission from GRBs in terms of the observed times and/or directions to the source of the neutrinos.

Such investigation has already been initiated by Nagataki and Kohri (2001), who computed the neutrino luminosity and its detectability, properly considering the time evolution of the central BH. Their calculations are based not on the merger models but on the collapsar model, and they adopt the simple analytical fitting formula to the hyper-critical (slim) disk model taken from Fujimoto et al. (2001). (Basic numbers are in good agreement with those obtained by the numerical evaluations by Popham et al 1999.) Their conclusion is that we will be able to marginally detect the neutrinos from collapsars occurring with “TITAND,” a next-generation multi-megaton water Cherenkov detector (Suzuki 2001). The first phase of TITAND is planned to be with 2 Mt water inside. In addition, we will be also able to know the direction to the source of neutrinos in TITAND. For the total number of emitted $\bar{\nu}_e$, we roughly evaluate

$$N_{\bar{\nu}_e} \sim \frac{\dot{q}_{Ne} V \Delta t}{\bar{E}_{\bar{\nu}_e}} \quad (75)$$

$$\sim 10^{57} \left(\frac{\dot{q}_{Ne}}{10^{35} \text{erg cm}^{-3} \text{s}^{-1}} \right) \left(\frac{\bar{E}_{\bar{\nu}_e}}{10 \text{MeV}} \right)^{-1} \left(\frac{V}{10^{20} \text{cm}^3} \right) \left(\frac{\Delta t}{10^{-3} \text{s}} \right), \quad (76)$$

with their mean energy $\bar{E}_{\bar{\nu}_e}$ to be emitted during one GRB event, where \dot{q}_{Ne} is estimated at $T \simeq 10 \text{MeV}/k_B$ and $\rho = 10^{13} \text{g cm}^{-3}$, V is the volume of the emitting region, and Δt is the duration. For the event number of $\bar{\nu}_e$'s,

$$R_{\text{event}} \sim 10 \left(\frac{d}{3 \text{Mpc}} \right)^{-2} \left(\frac{N_{\bar{\nu}_e}}{10^{57}} \right) \left(\frac{\bar{E}_{\bar{\nu}_e}}{10 \text{MeV}} \right)^2 \left(\frac{V_{\text{H}_2\text{O}}}{2 \text{Mt}} \right) \quad (77)$$

will be detected by TITAND, where d is the distance from the source and $V_{\text{H}_2\text{O}}$ is the volume of water. Hence, we optimistically expect to detect neutrinos from NDAFs, if GRB occurs within a distance of 3 Mpc. If detected, neutrino signals and correlations with GRB will be able to make clear the unknown explosion mechanism of GRBs. In order to derive the reliable estimations on neutrino flux, however, we should perform detailed computations as was done by Nagataki and Kohri (2001). This is left as future work.

4. Conclusion

We study the properties of hyper-critical accretion flow and for surface density exceeding about 10^{20}g cm^{-2} , which realizes when about a solar mass material is contained within a disk with a size of $\sim 5 \times 10^6 \text{cm}$, we find the following unique features:

1. Radiation luminosity of such flow is practically zero due to significant photon trapping, although mass accretion rate enormously exceeds the critical rate, $\dot{M} \gg L_{\text{Edd}}/c^2$.
2. Neutrino-cooling dominates over advective cooling. Thus the flow can cool via neutrino emission. We expect to detect neutrinos from GRBs with the next-generation, multi-megaton water Cherenkov detector in future.
3. Electron degeneracy pressure dominates over gas and radiation pressure, and the degenerate electron definitely influences the processes of neutrino emission. This feature is distinct from that of the solution found by NPK.
4. The disks are stable both against thermal and viscous instabilities, even when we take into account electron degeneracy.
5. Magnetic field strength exceeds the critical value, even if we take only 0.1% of the equipartition value. Then, photon splitting may occur, producing significant number of photons of energy below ~ 511 keV, thereby possibly suppressing e^\pm pair creation. However, quantitative discussion is left as future work.

We are grateful to R. Narayan, Shoichi Yamada and S. Nagataki for useful discussions and comments. The comments by the anonymous referee are also suggestive and helpful in making the final draft. We also thank the Yukawa Institute for Theoretical Physics at Kyoto University for the YITP workshops YITP-W-01-13? on “Gamma-Ray Bursts,” and YITP-W-01-17 on “Black Holes, Gravitational Lens, and Gamma-Ray Bursts,” in which this work was initiated and completed. This work was supported in part by the Grants-in Aid of the Ministry of Education, Science, Sports, and Culture of Japan (13640238, SM). Numerical computation in this work was carried out at the Yukawa Institute Computer Facility.

REFERENCES

Abramowicz, M.A., Czerny, B., Lasota, J.P., Szuszkiewicz, E. 1988, ApJ, 332, 646

Adler, S.L. 1971, Ann. Phys, 67, 599

Agol, E., Krolik, J., Turner, N.J., & Stone, J.M. 2001, ApJ, 558, 543

Bethe, H.A. 1993, ApJ, 412, 192

Burrows, A., Young, T., Pinto, P., Eastman, R., & Thompson, T.A. 2000, ApJ, 539, 865

Chevalier, R. 1996, ApJ, 459, 322

Chistyakov, M.V., Kuznetsov, A.V., & Mikheev, N.V. 1998, Phys. Lett. B, 434, 67

Eichler, D., Livio, M., Piran, T., & Schramm, D.N. 1989, *Nature*, 340, 126

Eggum, G.E., Coroniti, F.V., & Katz, J.I 1988, *ApJ*, 330, 142

Fryer, C.L., & Woosley, S. E. 1998, *ApJ*, 502, L9

Fryer, C.L., Woosley, S.E., Herant, M., & Daview, M.B. 1999, *ApJ*, 520, 650

Fujita, M., & Okuda, T. 1998, *PASJ*, 50, 639

Fujimoto, S., Arai, K., Matsuba, R., Hashimoto, M., Koike, O., & Mineshige, S. 2001, *PASJ*, 53, 509

Goodman, J. 1986, *ApJ*, 308, L47

Hannestad, S. & Raffelt, G. 1998, *ApJ*, 507, 339

Igumenshchev, I.V., Abramowicz, M.A., & Narayan, R. 2000, *ApJ*, 537, L27

Ishizuka, C., Ohnishi, A., & Sumiyoshi, K. 2002, *nucl-th/0201026*

Itoh, N., Adachi, T., Nakagawa, M., Kohyama, Y., & Munakata, H. 1989, *ApJ*, 339, 354

Itoh, N., Adachi, T., Nakagawa, M., Kohyama, Y., & Munakata, H. 1990, *ApJ*, 360, 741

Kato, S., Fukue, J., & Mineshige, S. 1998, *Black-Hole Accretion Disks*, Kyoto Univ. Press

Kohri, K., & Yamada, S. 2002a, *Phys. Rev. D* 65, 043006

—————. 2002b, in preparation

Kudoh, T., Matsumoto, R., & Shibata, K. 1998, *ApJ*, 508, 186

MacFadyen, A. I., & Woosley, S.W. 1999, *ApJ*, 524, 262

Mészáros, P. 1992, *High Energy Radiation from Magnetized Neutron Stars* (U. Chicago Press, Chicago), p.30

Mészáros, P. 2001, *Science*, 291, 79

Mészáros, P., Rees, M.J., & Wijers, R. 1999, *New Astron.* 4, 313

Melrose, D.B., & Stoneham, R.J. 1976, *Nuovo Cimento*, 32, 435

Nagataki, S., & Kohri, K. 2001, submitted to *Prog. Theor. Phys.*

Narayan, R., Igumenshchev, I.V., & Abramowicz, M.A., 2000, *ApJ*, 539, 798

Narayan, R., Paczyński B., Piran T. 1992, *ApJ* 395, L83

Narayan, R., Piran T., Kumar P. 2001, ApJ 557, 949 (NPK)

Paczynski, B. 1986, ApJ, 308, L43

Paczynski, B. 1991, Acta Astron., 41, 257

Paczynski, B. 1998, ApJ, 494, L45

Piran, T. 2000, Physics Reports, 333, 529

Popham, R., Woosley, S.E., & Fryer, C. 1999, ApJ, 528, 356

Quataert, E., & Gruzinov, A. 2000, ApJ, 539, 809

Rees, M.J., & Mészáros, P., 1992, MNRAS, 258, p41

Rees, M.J., & Mészáros, P., 1994, ApJ, 430, L93

Ruffert, M., & Janka, H.-Th. 1999, A&A, 24, 337

Ruffert, M., Janka, H.-Th. & Schäfer 1996, A&A, 311, 532

Ruffert, M., Janka, H.-Th., Takahashi, K.& Schäfer 1997, A&A, 319, 122

Shabad, A.E. 1975, Ann. Phys., 90, 1975

Shen, H., Toki, H., Oyamatsu, K. & Sumiyoshi, K. 1998, Prog. Thor. Phys., 100, 1013.

Shinder, P.J., Schramm, D.N., Wiita, P.J., Margolis, S.H. & Tubbs, D.L. 1987, ApJ, 313, 531

Spruit, H.C. 1999, A& A, 341, L1

Suzuki, Y. 2001, hep-ex/0110005

Thompson, C. 1994, MNRAS, 270, 480

Usov, V.V. 1992, Nature, 357, 472

Usov, V.V. 1994, MNRAS, 267, 1035

Wijers, R., & Galama, T. 1999, ApJ, 523, 177

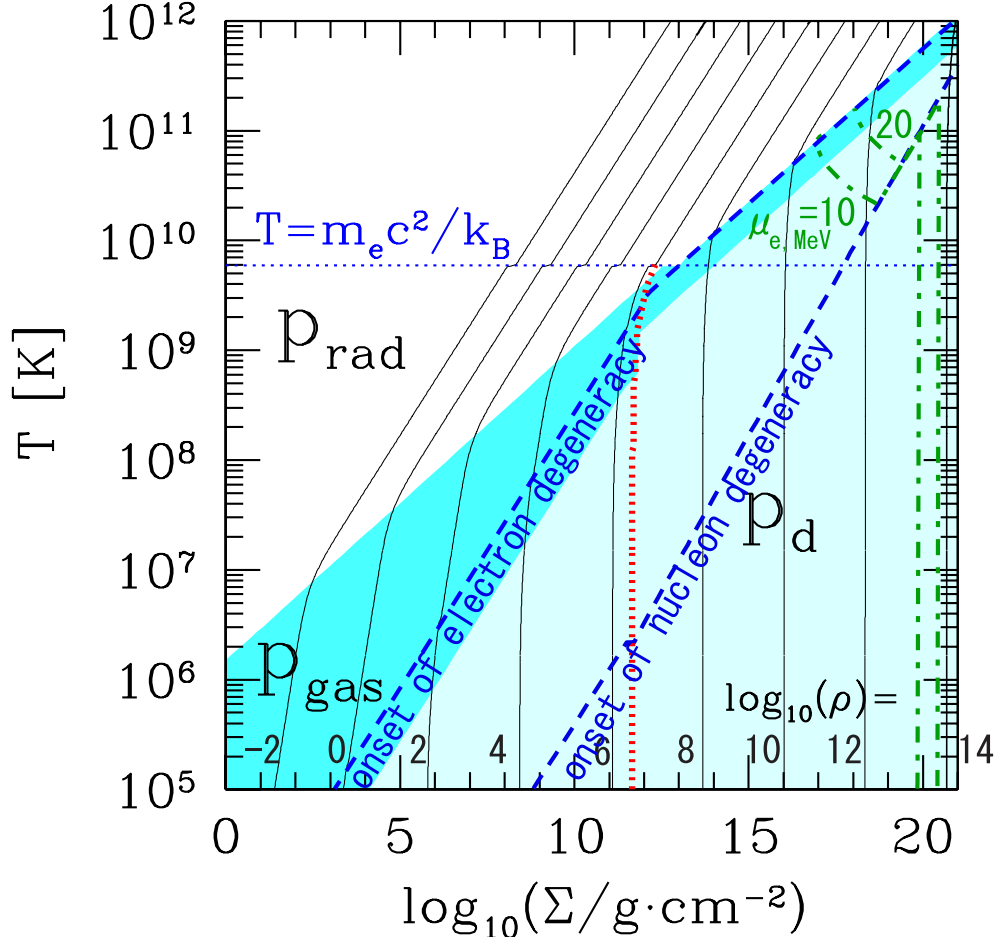


Fig. 1.— Contours of the matter density on the (Σ, T) plane for case that the black-hole mass is $M_{\text{BH}} = 3 M_{\odot}$ and $r = 4 r_g$, where r_g is the Schwarzschild radius. The solid lines denote the contours of the matter density for $\log(\rho/\text{g cm}^{-3}) = -2, 0, 2, \dots, 14$. The dark (or light) shadowed region represents that p_{gas} (p_{d}) dominantly contributes to the total pressure, while the white region represents that p_{rad} is dominant. The left and right thick dashed lines, respectively, denote the loci where electron and nucleon degeneracy begin to take place. Namely, electrons (or nucleons) are degenerate because of higher density on the right side of the left (right) dashed line. The horizontal dotted line denotes the temperature which corresponds to the electron mass m_e . The thick dotted line denotes the boundary where electrons become relativistic due to higher energy density ($\rho \gtrsim 2 \times 10^6 \text{ g cm}^{-3}$) while $T \lesssim m_e c^2/k_B$. The dot-dashed lines represent the chemical potential of electron in units of MeV, $\mu_{e,\text{MeV}} = 10$, and 20 , from the lower left to the upper right.

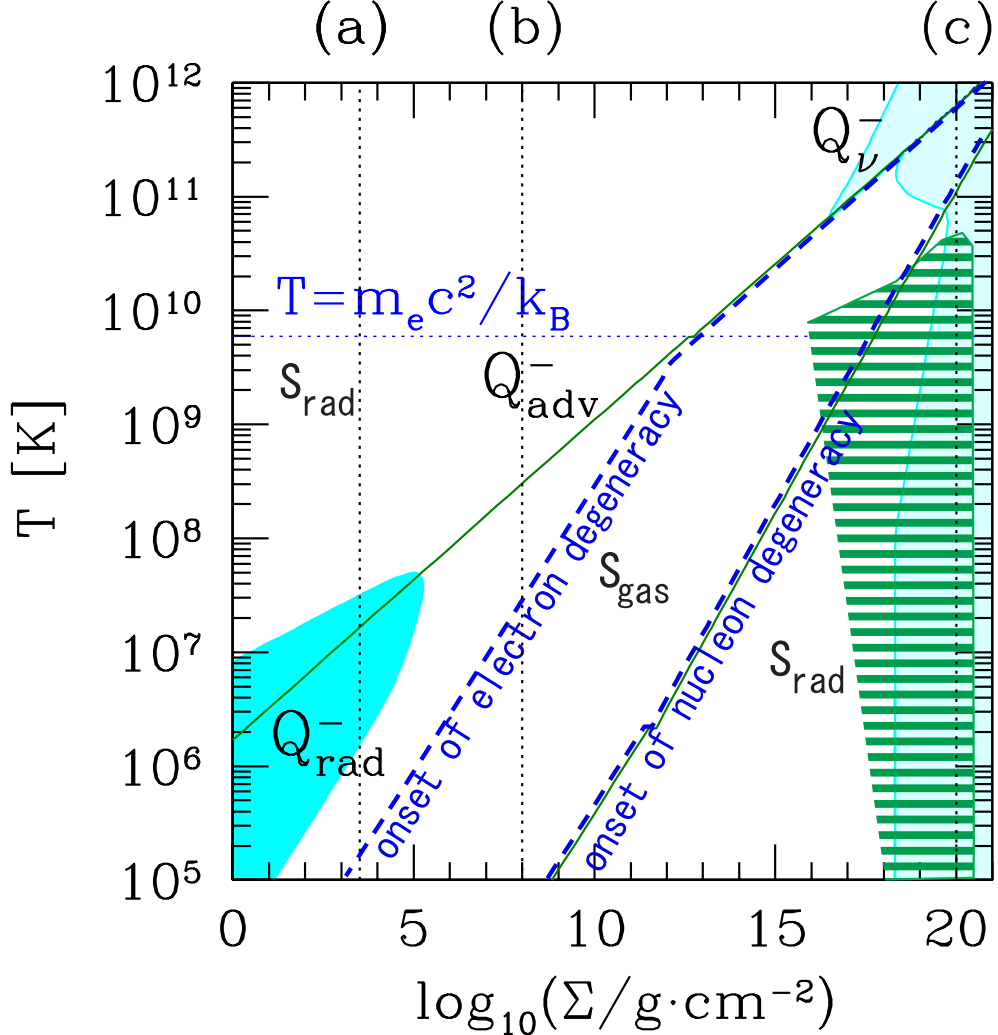


Fig. 2.— Plot of the most dominant component in the cooling rates on the (Σ, T) plane. The adopted parameters are the viscosity parameter, $\alpha = 0.1$, the black-hole mass, $M_{\text{BH}} = 3 M_{\odot}$, and $r = 4 r_g$. The dark (light) shadowed region and white region, respectively, represent the places where the radiative (neutrino) cooling and the advective cooling is the dominant process. On the other hand, the region between the two solid lines represents the place where the gas entropy s_{gas} mainly contributes to the total entropy. The striped region represents the place where heavy elements are produced, and there exist just a small amount of free nucleons. The vertical dotted lines, (a), (b), and (c) denote the representative values of Σ , at which heating and cooling rates are plotted in Fig. 3. The dashed and horizontal dotted lines are the same as those in Fig. 2.

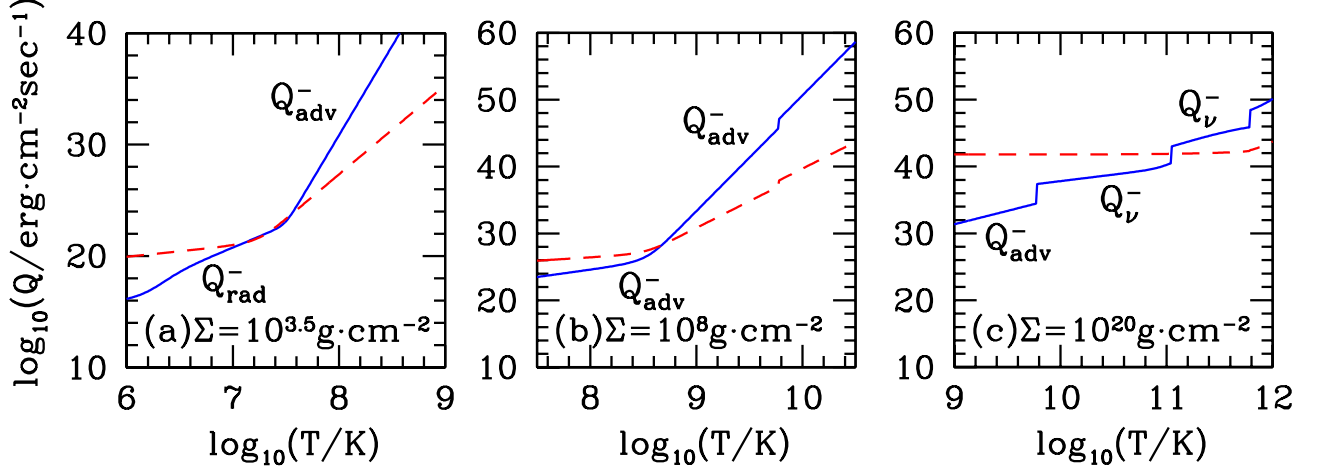


Fig. 3.— Heating and cooling rates as functions of temperature for a fixed surface density; from left to right, (a) $\Sigma = 10^{3.5} \text{ g cm}^{-2}$, (b) $\Sigma = 10^8 \text{ g cm}^{-2}$, and (c) $\Sigma = 10^{20} \text{ g cm}^{-2}$, respectively. The other parameters are the same as those in Fig. 2.

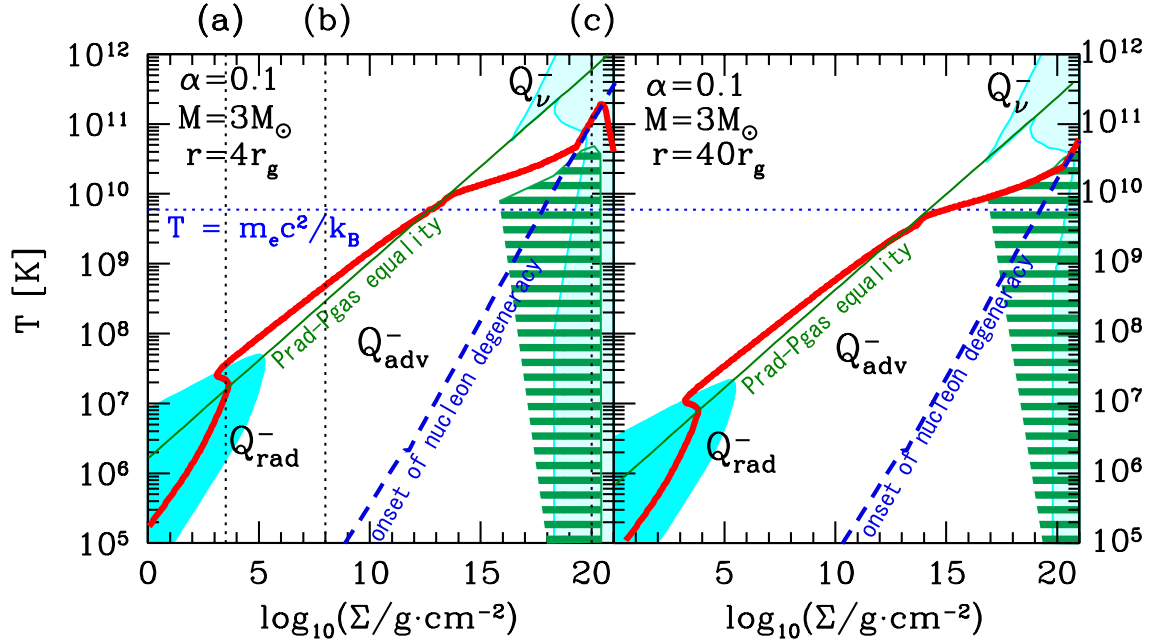


Fig. 4.— Thermal equilibrium curves (by the thick solid line) on the (Σ, T) planes at radial distances of $r = 4 r_g$ (left panel) and $r = 40 r_g$ (right panel). The adopted parameters are $\alpha = 0.1$ and $M_{\text{BH}} = 3 M_{\odot}$. The vertical dotted lines (a), (b), and (c) denote the three representative values of Σ adopted in plotting Fig. 3. The thin line indicates the loci where gas pressure equals radiation pressure. The dashed line indicates the loci where nucleon degeneracy sets out. We also indicate dominant source of cooling by shaded zone as in Fig. 2. In the striped region, there exist just a small amount of free nucleons, and the neutrino cooling does not work well.

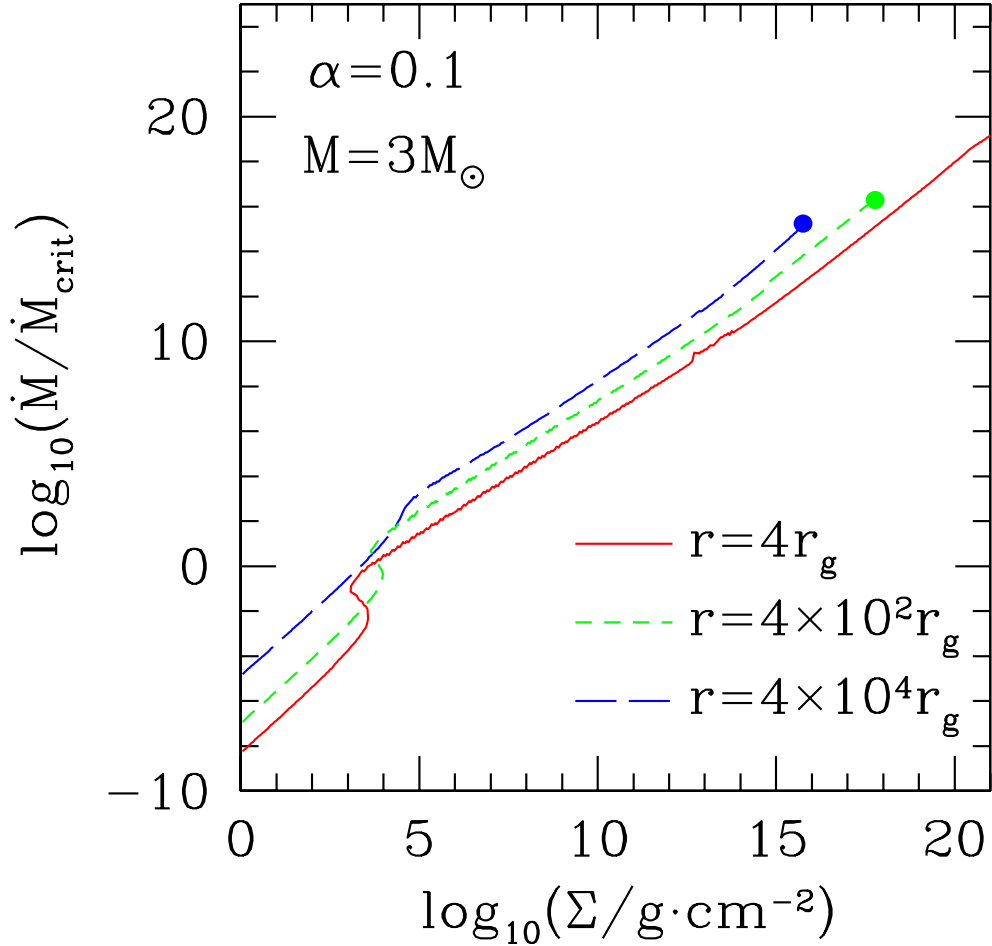


Fig. 5.— Thermal equilibrium curves on the (Σ, \dot{M}) plane at $r = 4 r_g$ (solid line), $400 r_g$ (dashed line), and $4 \times 10^4 r_g$ (long-dashed line). All other parameters are the same as those in Fig. 4. The solid circles at the upper ends indicate the places of $H = r$, above which no physical solution exists.

Table 1. T - Σ and \dot{M} - Σ Relations in Various Regimes

	p	Q^+	Q^-	T - Σ relation	\dot{M} - Σ relation
I	p_{gas}	$\alpha \Sigma T r^{-\frac{3}{2}} M_{\text{BH}}^{\frac{1}{2}}$	$Q_{\text{rad}}^- \propto \Sigma^{-1} T^4$	$\alpha^{\frac{1}{3}} \Sigma^{\frac{2}{3}} r^{-\frac{1}{2}} M_{\text{BH}}^{\frac{1}{6}}$	$\alpha^{\frac{4}{3}} \Sigma^{\frac{5}{3}} r M_{\text{BH}}^{-\frac{1}{3}}$
II	p_{rad}	$\alpha \Sigma^{-1} T^8 r^{\frac{3}{2}} M_{\text{BH}}^{-\frac{1}{2}}$	$Q_{\text{rad}}^- \propto \Sigma^{-1} T^4$	$\alpha^{-\frac{1}{4}} \Sigma^0 r^{-\frac{3}{8}} M_{\text{BH}}^{\frac{1}{8}}$	$\alpha^{-1} \Sigma^{-1} r^{\frac{3}{2}} M_{\text{BH}}^{-\frac{1}{2}}$
III	p_{rad}	$\alpha \Sigma^{-1} T^8 r^{\frac{3}{2}} M_{\text{BH}}^{-\frac{1}{2}}$	$Q_{\text{adv}}^- \propto \alpha \Sigma^{-3} T^{16} r^{\frac{11}{2}} M_{\text{BH}}^{-\frac{5}{2}}$	$\alpha^0 \Sigma^{\frac{1}{4}} r^{-\frac{1}{2}} M_{\text{BH}}^{\frac{1}{4}}$	$\alpha \Sigma r^{\frac{1}{2}} M_{\text{BH}}^{\frac{1}{2}}$
IV	$p_{\text{d,rel}}^{\dagger}$	$\alpha \Sigma^{\frac{9}{7}} r^{-\frac{27}{14}} M_{\text{BH}}^{\frac{9}{14}}$	$Q_{\text{adv}}^- \propto \alpha \Sigma T^2 r^{-\frac{1}{2}} M_{\text{BH}}^{-\frac{1}{2}}$	$\alpha^0 \Sigma^{\frac{1}{7}} r^{-\frac{5}{7}} M_{\text{BH}}^{\frac{4}{7}}$	$\alpha \Sigma^{\frac{9}{7}} r^{\frac{15}{14}} M_{\text{BH}}^{-\frac{5}{14}}$
V	$p_{\text{d,rel}}$	$\alpha \Sigma^{\frac{9}{7}} r^{-\frac{27}{14}} M_{\text{BH}}^{\frac{9}{14}}$	$Q_{\nu}^- \propto \eta_e^9 T^9 \Sigma^{\frac{1}{7}} r^{\frac{9}{7}} M_{\text{BH}}^{-\frac{3}{7}}$	$\Sigma^{\frac{4}{7}} r^{-\frac{6}{7}} M_{\text{BH}}^{\frac{2}{7}}$	$\alpha \Sigma^{\frac{9}{7}} r^{\frac{15}{14}} M_{\text{BH}}^{-\frac{5}{14}}$

[†]Here p_{gas} also contributes to the pressure secondly and induces the T -dependence in Q_{adv}^- .